



From local to regional compound flood mapping with deep learning and data fusion techniques



David F. Muñoz ^{a,b,*}, Paul Muñoz ^c, Hamed Moftakhari ^{a,b}, Hamid Moradkhani ^{a,b}

^a Department of Civil, Construction and Environmental Engineering, The University of Alabama, Tuscaloosa, AL 35487, United States

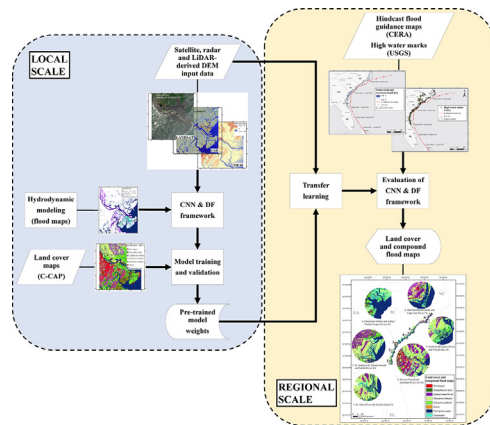
^b Center for Complex Hydrosystems Research, The University of Alabama, Tuscaloosa, AL 35487, United States

^c Departamento de Recursos Hídricos y Ciencias Ambientales, Universidad de Cuenca, Cuenca 010150, Ecuador

HIGHLIGHTS

- Deep learning and fusion framework is used for large-scale compound flood mapping.
- Compound flood maps agree well with those of the Coastal Emergency Risk Assessment.
- The framework matches the location of USGS – high water marks in coastal counties.
- Transfer learning from local to large-scale is suitable for compound flood mapping.
- The framework can contribute to efforts in calibration of hydrodynamic models.

GRAPHICAL ABSTRACT



ARTICLE INFO

Article history:

Received 8 February 2021

Received in revised form 29 March 2021

Accepted 30 March 2021

Available online 6 April 2021

Editor: Fernando A.L. Pacheco

Keywords:

Compound flood mapping

Convolutional neural networks

Data fusion

Deep learning

Hurricanes

ABSTRACT

Compound flooding (CF), as a result of oceanic, hydrological, meteorological and anthropogenic drivers, is often studied with hydrodynamic models that combine either successive or concurrent processes to simulate inundation dynamics. In recent years, convolutional neural networks (CNNs) and data fusion (DF) techniques have emerged as effective alternatives for post-flood mapping and supported current efforts of complex physical and dynamical modeling. Yet, those techniques have not been explored for large-scale (regional) compound flood mapping. Here, we evaluate the performance of a CNN & DF framework for generating CF maps along the southeast Atlantic coast of the U.S. as a result of Hurricane Matthew (October 2016). The framework fuses multispectral imagery from Landsat analysis ready data (ARD), dual-polarized synthetic aperture radar data (SAR), and coastal digital elevation models (DEMs) to produce flood maps at moderate (30 m) spatial resolution. The highest overall accuracy (97%) and f1-scores of permanent water/floodwater (99/100%) are achieved when ARD, SAR and DEM datasets are readily available and fused. Moreover, the resulting CF maps agree well (80%) with hindcast flood guidance maps of the Coastal Emergency Risk Assessment and can effectively match post-flood high water marks of the U.S. Geological Survey distributed in coastal counties. We ultimately evaluate the framework with different DF alternatives and highlight their usefulness for large-scale compound flood mapping as well as calibration of hydrodynamic models. The cost-effective approach proposed here enables efficient estimation of exposure to compound coastal flooding and is particularly useful in data scarce regions.

© 2021 Elsevier B.V. All rights reserved.

* Corresponding author at: Department of Civil, Construction and Environmental Engineering, The University of Alabama, Tuscaloosa, AL 35487, United States.
E-mail address: dfmunoz1@crimson.ua.edu (D.F. Muñoz).

1. Introduction

Compound flooding (CF) is a natural hazard resulting from either successive or concurrent flood drivers (e.g., storm surge, river discharge and/or rainfall) with associated socio-economic and environmental impacts that can be larger than those produced by each driver in isolation (Bevacqua et al., 2020; Moftakhari et al., 2017; Wahl et al., 2015; Zscheischler et al., 2020). CF poses a significant threat to life and assets of people settled in low-lying coasts including riverine floodplains and estuarine zones at local (Klerk et al., 2015; Olbert et al., 2017; Wang et al., 2018), regional (Bevacqua et al., 2019; Fang et al., 2020; Hendry et al., 2019; Wu et al., 2018), and global scale (Couasnon et al., 2020; Eilander et al., 2020; Ward et al., 2018). In the East and Gulf coasts of United States, CF is mainly triggered by tropical cyclones producing wind-driven storm-surge and heavy rainfall (Gori et al., 2020; Muis et al., 2019; Song et al., 2020), with inherent risks higher than those of the Pacific coast (Wahl et al., 2015).

Among the costliest hurricanes that made landfall in the southeast Atlantic coast of the U.S., Hurricane Matthew (October 2016) was responsible for 34 deaths and more than 3 million residents evacuated from coastal areas (Stewart, 2017). Although minor damages to roofs, pools and line utilities were associated to the direct wind force, storm-surge caused severe structural damages with maximum inundation depths greater than 2 m above ground from Florida to North Carolina. Moreover, the compounding effects of pluvial and coastal flooding resulted in electrical power outages, and approximately \$10 billion of wind- and water-related damages according to the National Centers for Environmental Information (NCEI) of the National Oceanic and Atmospheric Administration (NOAA). Compound flood inundation mapping is therefore of paramount importance for emergency planners and stakeholders, as they require these maps for decision-making and rapid coastal flood assessment.

Flood inundation maps are commonly obtained from advanced hydrodynamic models that simulate complex oceanic, hydrological, meteorological and anthropogenic processes with a robust numerical scheme. The advanced circulation model (ADCIRC) (Luettich et al., 1992) and DELFT3D (Roelvink and Van Banning, 1995) are among the high-performance hydrodynamic models that have been used for large-scale modeling studies in the U.S. (Dietrich et al., 2011; Martyr-Koller et al., 2017; Muis et al., 2019; Thomas et al., 2019). Particularly, ADCIRC provides real-time flood forecasts as well as hindcast flood guidance maps of the Atlantic and Gulf coast through the Coastal Emergency Risk Assessment (CERA) web mapper (<https://cera.coastalrisk.live/>). In spite of the growing access to powerful and low-cost computational resources, physically-based modeling approaches are still computationally intensive and often require model domain partitioning and parallelization tasks to map flood extent at large-scale (Dietrich et al., 2012, 2011).

An alternative for efficient post-event large-scale flood mapping is the application of remote sensing techniques to multispectral imagery, radar data and digital elevation models (DEMs). These datasets allow for delineating flood extent over large areas in near real-time depending on the satellite's revisit time and/or spatiotemporal resolution. Multispectral imagery and DEM datasets have been successfully combined for flood mapping in riverine and coastal floodplains with diverse techniques including principal component analysis, logical filtering, decision rules and image segmentation (Cohen et al., 2019; Gianinetto et al., 2006; Wang et al., 2002). Contrary to multispectral imagery, the applicability of backscattering radar data is not limited by adverse atmospheric conditions (e.g., shadows or cloud formation) as the radar antenna can emit and receive oscillating signals even during nighttime conditions (Flores-Anderson et al., 2019). This in turn makes radar data a powerful resource for flood mapping in urban settings and natural landscapes (Liang and Liu, 2020; Liu et al., 2019).

Integration of backscattering radar data with either multispectral imagery or DEMs has been proposed for coastal flood monitoring and

mapping with different techniques including change detection analysis, threshold-based and probabilistic approaches (Anusha and Bharathi, 2020; Chaouch et al., 2012; Clement et al., 2018; Martinis et al., 2013). Among the machine learning techniques used for flood mapping, artificial neural networks (Singh and Singh, 2017; Tam et al., 2019; Tien Bui et al., 2020), support vector machine (Dhara et al., 2020; Nandi et al., 2017), and random forest (Feng et al., 2015; Kabir et al., 2020a) have improved the accuracy of flood maps due to their ability to learn local features from terrain, soil properties and spectral indices (Huang et al., 2017; Rad et al., 2021; Zoka et al., 2018), radar intensity and interferometric coherence properties (Canisius et al., 2019; Li et al., 2019), and time series analysis (DeVries et al., 2020; Lin et al., 2019). More advanced techniques, such as convolutional neural networks (CNNs), use a deep architecture allowing for optimal feature learning at low-, mid- and high- levels of abstraction (e.g., edges, objects, and patterns) and hence outperforming 'shallow' machine learning techniques in a variety of applications such as object detection and image segmentation (Hoeser et al., 2020; Pi et al., 2020), land cover classification (Li et al., 2018; Mahdianpari et al., 2018; Muñoz et al., 2021), and flood mapping (Gebrehiwot et al., 2019; Li et al., 2019; Sarker et al., 2019).

Despite the benefits of the aforementioned techniques that focus on binary classification, i.e., flood and non-flood areas, there are no studies that integrate multi-source satellite-based data, hydrodynamic modeling, deep learning (DL) and data fusion (DF) techniques for large-scale land cover classification and compound flood mapping. The advantage of conducting multiclass land cover classification including flood inundation mapping relies on the ability of DL models to learn complex spatial patterns (Dalponte et al., 2008; Mahdianpari et al., 2018; Rezaee et al., 2018), and therefore separate purely hurricane-induced and pluvial flooding from periodical flooding in coastal areas (e.g., wetlands, salt marshes and mangroves). DL models such as CNNs can effectively delineate permanent water bodies and non-inundated urban areas (Hoeser et al., 2020; Xu et al., 2019), and hence expediting flood hazard assessments and emergency responses in flood prone areas. In contrast, binary classification of flood/non-flood areas require additional steps to identify permanent water bodies based on existing land cover maps (if available) as well as adequate threshold values that help discriminate water from land features. This is turn compromises the accuracy of flood maps since a single threshold value might not account for land surface complexity and variability (Liang and Liu, 2020), and consequently fail to effectively map CF.

In this context, we modified a previously developed CNN & DF framework (Muñoz et al., 2021) to conduct multi-class land cover classification with floodwater samples obtained from a physically-based model. The framework fuses multispectral Landsat analysis ready data (ARD), dual-polarized synthetic aperture radar data (SAR) and light detection and ranging (LiDAR) coastal DEMs to generate compound flood maps with moderate (30 m) spatial resolution. We first train the CNN & DF framework with official land cover maps as well as floodwater maps generated with a calibrated Delft3D-FM model of the Savannah River estuary (hereby referred as 'training area'). Then, we conduct transfer learning with conveniently stored model weights to further evaluate the framework in the southeast Atlantic coast of the U.S. We select Hurricane Matthew (October 2016) for training and evaluation purposes since this extreme event led to considerable flood extent and inundation depths in several estuaries, islands and bays.

2. Local and regional datasets

2.1. Study area

The study area comprises multiple rivers, estuaries, bays and islands located in the southeast Atlantic coast of the U.S. (Fig. 1a). From this large-scale study area, we define a strategical and local scale 'training area' along the Savannah River estuary that separates the states of Georgia and South Carolina (Fig. 2a). The training area is characterized

by complex geomorphological features and presents vast wetland regions of considerable ecological value as well as intense anthropogenic intervention that together shape a unique riverine-estuarine system (Reynolds, 2016; Seabrook, 2006). Another important aspect is that the training area is frequently monitored, and so counts with multi-source data including multispectral Landsat ARD imagery, SAR data, LiDAR-derived coastal DEMs, and high water marks of the U.S. Geological Survey (USGS) collected after extreme flooding events (e.g., Hurricane Matthew). Furthermore, the training area has been studied with a detailed and calibrated Delft3D-FM hydrodynamic model for extreme/non-extreme events including hurricane-induced (compound) flooding (Muñoz et al., 2020).

The path of Hurricane Matthew started along the southern coasts of Florida as a category 3 in the Saffir-Simpson scale (2016/10/07–06:00 UTC), and then weakened into category 2 and 1 along the northern coasts of Florida (2016/10/08–00:00 UTC) and South Carolina (2016/10/08–15:00 UTC), respectively (Fig. 1a). Furthermore, Hurricane Matthew considerably impacted the Savannah River estuary leading to the highest water surface level of the entire southeast Atlantic coast with 2.58 m at Fort Pulaski station (Fig. 3a, NOAA ID: 8670870). We thereby argue that the Savannah River estuary is a suitable study area to train the CNN & DF framework. Eventually, the framework will be evaluated in terms of compound flood mapping accuracy along the southeast Atlantic coast of the U.S.

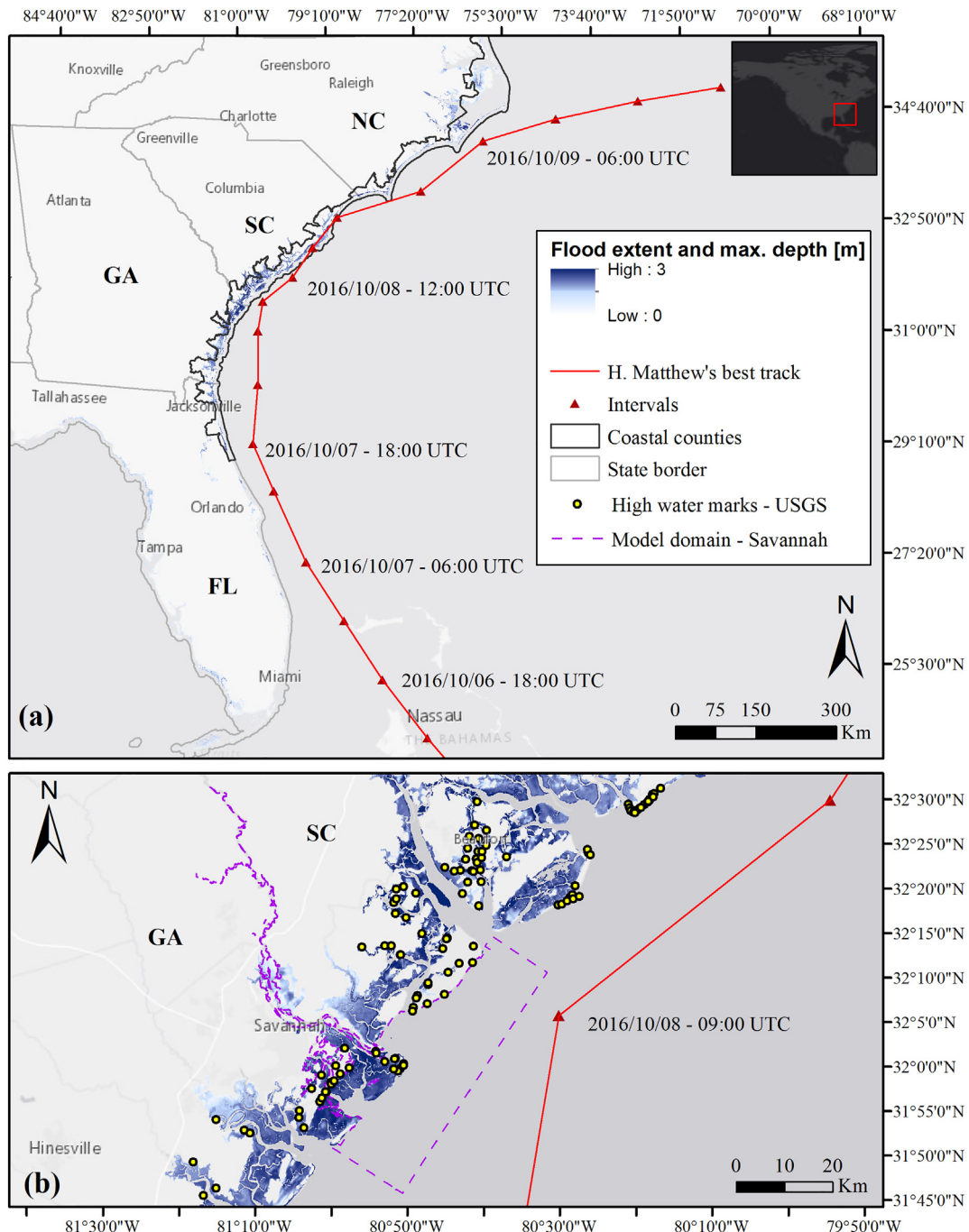


Fig. 1. Map of the southeast Atlantic coast of the U.S. and Hurricane Matthew (Oct/2016). (a) Flood extent and maximum inundation depth above ground (blue color scale) obtained from the CERA web mapper. Hurricane's best track (red solid line) and intervals (triangles) indicate the proximity and timing of the hurricane to the coast. (b) Map of Savannah River estuary (training area). USGS – high water marks (yellow circles) and Delft3D-FM model domain (purple dashed line) are used to train the CNN & DF framework.

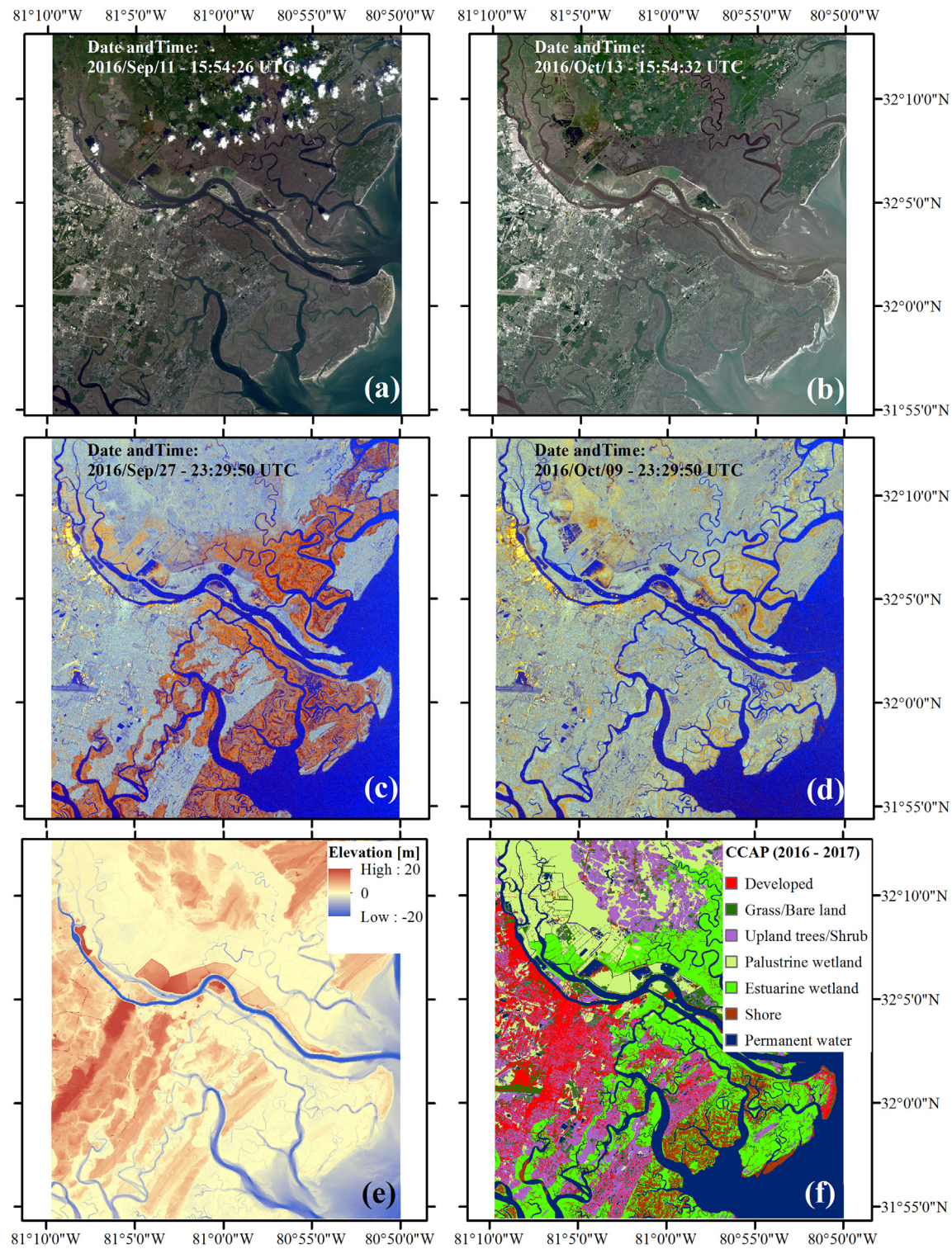


Fig. 2. Publicly available data of the Savannah River estuary used to train the CNN & DF framework. (a, b) Landsat ARD imagery with red, blue, and green band composite, and (c, d) SAR data with dual polarized VH, VV and VH/VH band composites showing pre- and post-flood conditions. (e) LiDAR derived coastal DEM of Savannah, GA. (f) C-CAP coastal land cover map for the period 2016–2017.

2.2. Data availability

Training, validation and evaluation of the CNN & DF framework is based on publicly available data from different sources. Landsat ARD imagery of moderate (30 m) spatial resolution is obtained from the Earth Explorer website (<https://earthexplorer.usgs.gov>). The advantage of using Landsat ARD over similar imagery products is that any effects of

atmospheric attenuation (e.g., scattering and absorption) on flood mapping accuracy are already corrected in the former product (Dwyer et al., 2018; Potapov et al., 2020). We use Landsat scenes with less than 20% of cloud cover and shadow as higher percentages might hinder the applicability of multispectral imagery to map CF (Fig. 2(a, b)). In addition, we use both Sentinel-1A and 1B (C-band) missions with dual-polarized radar data (e.g., vertical-horizontal (VH) and vertical-vertical (VV)

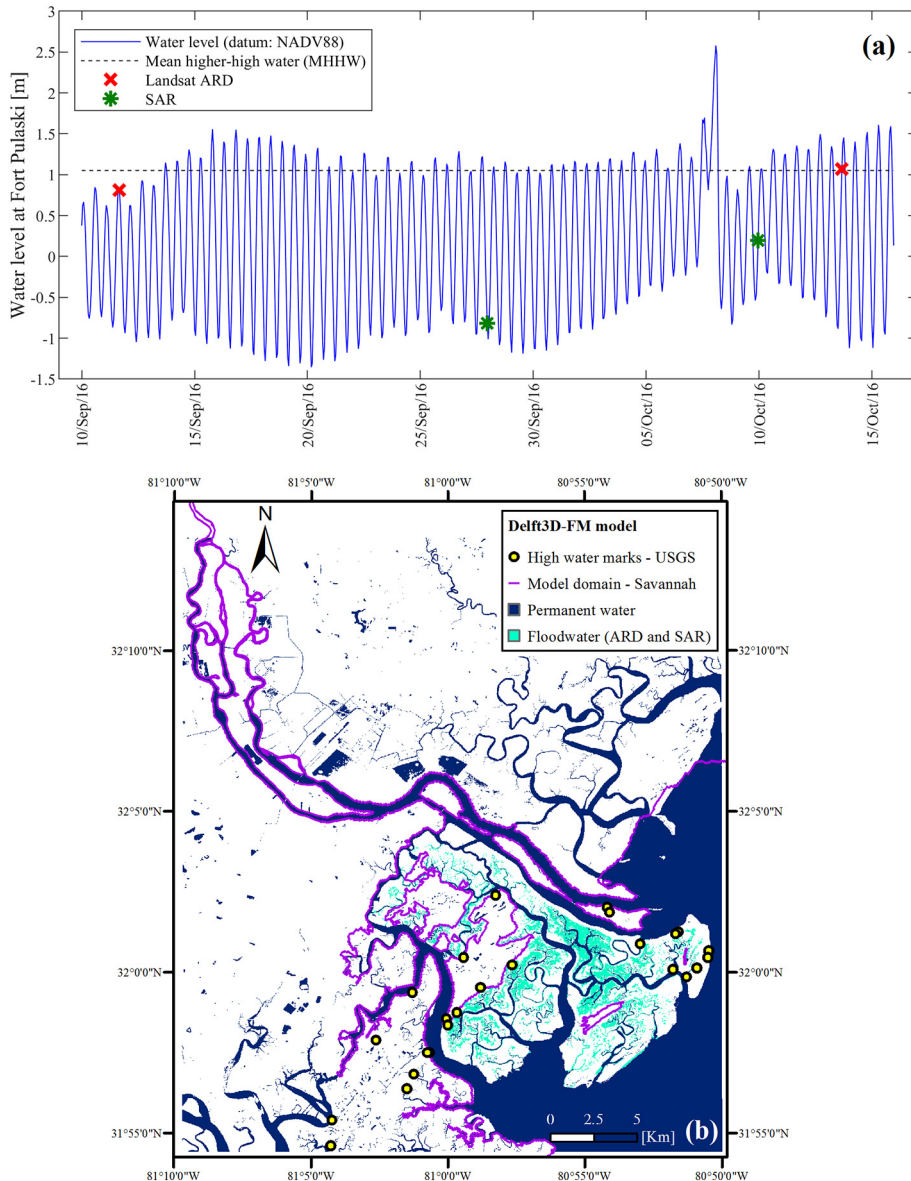


Fig. 3. Floodwater in Savannah River estuary above Mean higher-high water (MHHW) obtained from hydrodynamic simulations. (a) Water level time series (blue solid line) observed in Fort Pulaski station (NOAA ID: 8670870) and MHHW (gray dashed line) relative to NAVD88. Acquisition dates of Landsat ARD imagery (red crosses) and SAR data (green asterisks) during pre- and post-flooding conditions. (b) Floodwater delineation within the Delft3D-FM model domain (purple solid line). Flood extent depicts floodwater areas that match the date/time of SAR and ARD data acquisition (cyan). USGS – high water marks (yellow circles) show verified flood locations during Hurricane Matthew.

polarimetric channels), interferometric wide swath (IW) frames and ground range detected (GRD) products (Fig. 2(c, d)). SAR datasets of high (10 m) spatial resolution are obtained from archives of the Alaska Satellite Facility (ASF) website (<https://asf.alaska.edu/>).

LiDAR-derived coastal DEM is another key dataset that improves the classification accuracy and flood mapping when combined with satellite-based and/or aerial imagery (Carranza-García et al., 2019; Feng et al., 2019; Muñoz et al., 2021). The 2014 Continuously Updated Digital Elevation Model (CUDEM) is a topographic and bathymetric (topobathy) dataset with a ninth arc-second spatial resolution (~3.4 m) that spans the southeast Atlantic coast of the U.S (Fig. 2e). The CUDEM topobathy is obtained from the NOAA digital coast repository (https://coast.noaa.gov/htdata/raster2/elevation/NCEI_ninth_Topobathy_2014_8483/). In addition to those datasets, the CNN & DF framework is trained with land cover maps of the Coastal Change Analysis Program (C-CAP, Fig. 2f). The program monitors changes of coastal intertidal areas, wetlands and adjacent uplands with ancillary datasets as well as very high resolution

aerial imagery (1 m) of the National Agriculture Imagery Program (NAIP). Likewise, C-CAP produces land cover products for coastal regions of the U.S. every five years and can be obtained from the NOAA digital coast repository (<https://coast.noaa.gov/digitalcoast/tools/lca.html>). Lastly, we use USGS – high water marks of Hurricane Matthew to indirectly verify flood areas delineated with the framework. These data are available in the USGS – Flood event viewer platform (<https://stn.wim.usgs.gov/FEV/>). A detailed summary of the data used in this study is also presented in Table 1.

3. Integration of remote sensing data with hydrodynamic and deep learning models

3.1. Data pre-processing

As the first step, we removed all remaining clouds and shadows from Landsat ARD scenes (e.g., see Fig. 2a) with the *fmask v4.0* tool (Qiu et al.,

Table 1

Datasets used for compound flood mapping with the CNN & DF framework in the south-east Atlantic coast of the U.S.

Dataset	Resolution [m]	Scene date, time (UTC) ID/Row/Path	Bands ^a
Landsat Analysis Ready Data (ARD)	30	2016-Oct-13, 15:54:32 LC08_CU_026014/37/16 2016-Oct-13, 15:54:56 LC08_CU_026015/38/16 2016-Oct-13, 15:54:08 LC08_CU_027013/36/16	R, G, B, Nir, Swir1 and Swir2
Dual-polarized synthetic aperture radar (SAR)	10	2016-Oct-09, 23:29:00 S1A_IW_GRDH/94/48 2016-Oct-09, 23:29:25 S1A_IW_GRDH/99/48 2016-Oct-10, 23:20:33 S1B_IW_GRDH/100/150 2016-Oct-10, 23:20:58 S1B_IW_GRDH/105/150 2016-Oct-11, 23:13:41 S1A_IW_GRDH/108/77	VH and VV
LiDAR-derived Digital Elevation Model (DEM)	3	2014 CUDEM ^b	Single band

^a Red (R), Green (G), Blue (B), Near-infrared (Nir), Shortwave infrared (SWIR) 1 and 2.

^b Vertical (V) and horizontal (H) polarimetric channels. Continuously updated DEM – topobathy dataset.

2019b) and ArcGIS. The tool was initially set with default parameter values and then fine-tuned to identify obscured and cloudy pixels. Landsat ARD does not require any further atmospheric correction and has been widely used in many applications including time series analysis, land cover change assessment, and global land cover mapping (Muñoz et al., 2019; Potapov et al., 2020; Qiu et al., 2019a). We then prepare SAR data with the open-access Sentinel Application Platform (SNAP v8.0) as suggested in similar flood mapping studies (Liu et al., 2019; Uddin et al., 2019). For this purpose, we first import and geo-code the radar data with the 'Apply-Orbit-File' tool. The data is subsequently masked with a pre-defined vector-file that comprises the training and evaluation areas (see Section 2.1). We then radiometrically calibrate the masked data to remove over-brightening effects due to the radar sensor.

Next, we reduce the speckle noise effect, i.e., grainy appearance or 'salt and pepper' noise, to enable an unbiased analysis of SAR images. Similarly, we account for geometric distortions (e.g., foreshortening, layover and shadow) with the 'Terrain-Correction' tool and the high resolution CUDEM topobathy data (Table 1). Also, we co-register the SAR images of pre- and post-flood conditions (Fig. 2(c, d)) with 5000 ground control points. These SAR images are ultimately used to train the CNN & DF framework. The SAR pre-processing steps are automated with the 'Graph Builder' option of SNAP and runs in batch mode. Similar to Muñoz et al. (2021), we resample all datasets to a pixel resolution of 5 × 5 m with the nearest neighbor method, and then re-scale the Landsat ARD and DEM data values to a range of 0 to 1. SAR data is already transformed to the dB scale (Eq. (1)), and therefore no additional scaling is done with this dataset.

3.2. Hydrodynamic modeling

We conduct model simulations with Delft3D-FM to identify floodwater areas in the Savannah River estuary after the peak surge of Hurricane Matthew (Fig. 3a). The hydrodynamic model was previously calibrated and validated with extreme and non-extreme events including compound flooding events as a result of Hurricane Matthew (Muñoz et al., 2020). Savannah floodplain consists of wetland and salt marsh regions that are periodically inundated by local tidal dynamics (i.e., M₂-semidiurnal tidal cycle). Thus, we first define a threshold value to distinguish purely hurricane-induced and/or fluvial flooding from periodic inundation of wetlands and salt marsh areas. The mean

higher-high water (MHHW) referenced to the North American Vertical Datum of 1988 (NAVD88) is here used as a threshold value (1.05 m) in this regard (Fig. 3a). MHHW is obtained from the NOAA's Tide & Currents website (<https://tidesandcurrents.noaa.gov/>) and seen as a proxy of inundation threshold according to the National Weather Service (NWS). Furthermore, MHHW has been used as a reference for nuisance tidal flooding in others studies (Moftakhari et al., 2015, 2018; Sweet et al., 2018).

Second, we generate flood maps with the hydrodynamic model that match the date/time of SAR and Landsat ARD data acquisition (Fig. 2(b, d)). Floodwater areas that spatially coincide in both flood maps are selected and grouped into a new land cover class named 'floodwater'. The floodwater class will be eventually associated with multispectral, backscattering and elevation features (above the MHHW threshold), and thus differentiating them from those of open and/or permanent water (Fig. 3b). Note that the maximum coastal water level at Fort Pulaski was ~1.5 m above MHHW. In that regard, we develop an alternative for compound flood mapping based on deep learning and/or multi-class land cover classification with floodwater samples explicitly derived from hydrodynamic modeling. The latter aims at improving flood mapping strategies that commonly rely on binary classification of flood/non-flood areas via multispectral and terrain indices, change detection, thresholds and object-based approaches (Chini et al., 2017; Huang et al., 2017; Liang and Liu, 2020; Munasinghe et al., 2018; Uddin et al., 2019).

3.3. Convolutional neural network and data fusion framework

The CNN & DF framework is developed in TensorFlow (www.tensorflow.org) and was used to analyze long-term wetland dynamics in a previous study with satisfactory results (Muñoz et al., 2021). In broad terms, the CNN model resembles the (winner) Fusion-FCN architecture of the 2018 IEEE GRSS Data Fusion Contest (Xu et al., 2019), and integrates a novel adaptive feature-fusion approach for multisource data (Feng et al., 2019). In this study, we extend the CNN & DF framework to account for SAR data and flood maps derived from a calibrated 2D hydrodynamic modeling (Muñoz et al., 2020). The framework consists of a tri-branch CNN architecture that simultaneously processes Landsat ARD, DEM and NAIP data, and can additionally incorporate other datasets in new or existing branches. Specifically, we adapt the framework to process SAR data instead of NAIP imagery since the latter is best suited for vegetation mapping (Maxwell et al., 2017). Likewise, we train the framework with C-CAP and floodwater maps generated with a detailed hydrodynamic model (see Section 3.2 for details). In broad terms, the framework resembles a fully-connected CNN (Xu et al., 2019) with an adaptive feature-fusion approach for optimal DF (Feng et al., 2019). The left branch is initially devised to extract spatial-spectral features from blue, green, red, near-infrared and short-wave infrared (1 and 2) bands, and then optimized to process selected band combinations reducing the computation burden (see Section 4.1 for details). The middle branch extracts spatial-elevation features from LiDAR-derived DEM data of single bands whereas the right branch extracts spatial-backscattering features converted from a linear to decibel (dB) scale (Eq. (1)).

$$\sigma_{\text{dB}}^0 = 10 \log_{10}(\sigma^0) \quad (1)$$

where, σ^0 and σ_{dB}^0 are the raw amplitude values and log-transformed backscattering SAR data, respectively.

The branches extract feature information from patch images of 30 × 30 pixels via two-dimensional convolution, rectified linear unit and average pooling operations. The resulting pooling layers are merged through point-wise addition to integrate low-, mid- and high- levels of abstraction, and hence benefit from multi-scale properties along each branch. Feng et al. (2019) proposed a novel alternative for DF of multisource hyperspectral imagery and LiDAR data based on

“Squeeze-and-Excitation Networks” (Hu et al., 2018). The alternative consists in an adaptive feature-fusion approach that computes the contribution of each feature to the classification task, and thereby fusing multisource features in a more intelligent fashion than simply feature stacking. The adaptive feature-fusion approach requires a two-

dimensional global average pooling layer, two fully connected layers and a “sigmoid” function (Feng et al., 2019; Muñoz et al., 2021), and produces an output tensor containing the global contribution (or feature weights) of Landsat imagery, SAR data and LiDAR-derived DEM to the land cover classification and compound flood mapping task. The

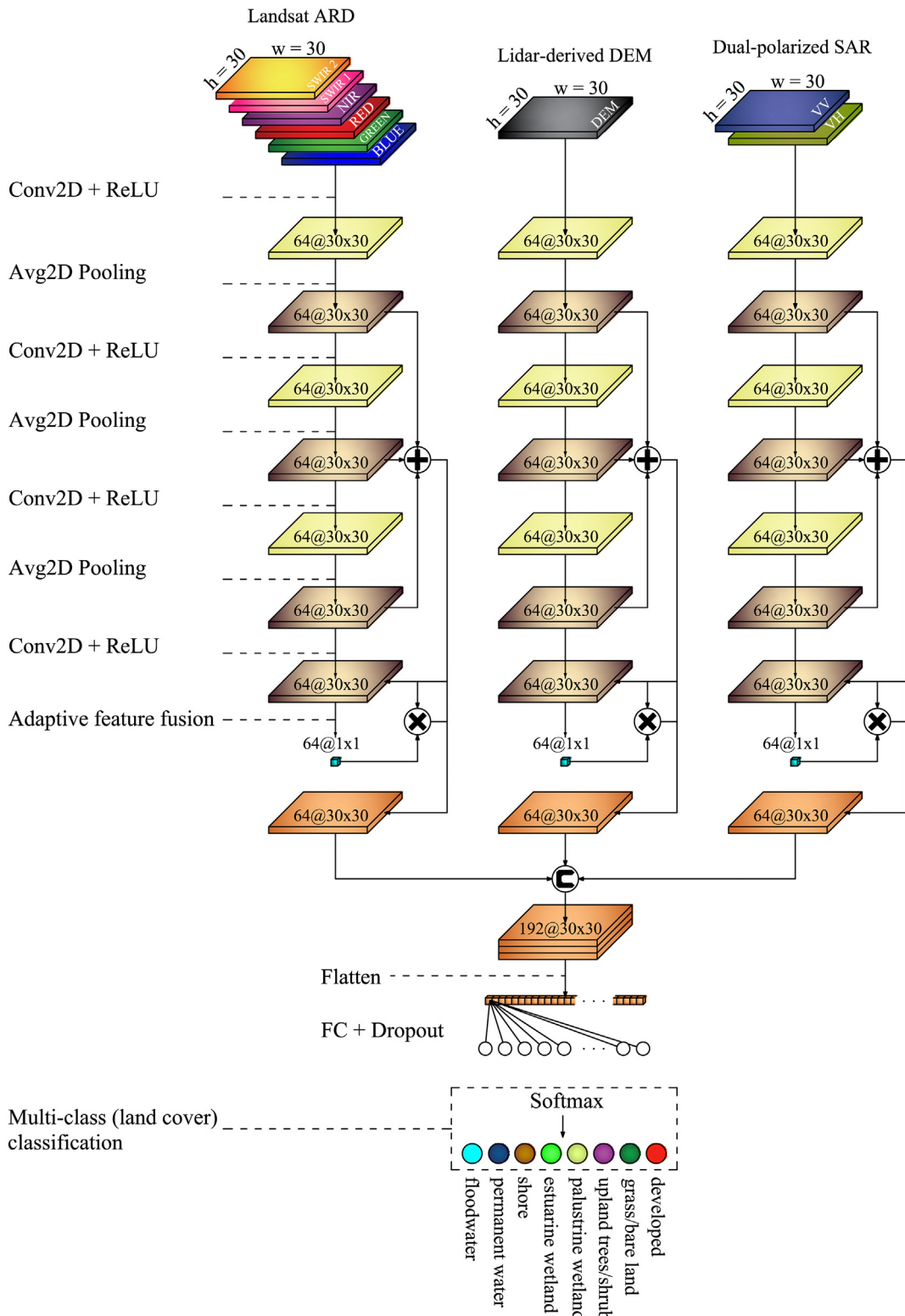


Fig. 4. Land cover and flood mapping model based on convolutional neural networks (CNN) and multisource data fusion (DF). The model consists of a tri-branch CNN with two-dimensional (2D) convolution (Conv), rectified linear unit (ReLU) and average (Avg) pooling operations. Avg2D pooling layers are merged into a single layer through point-wise addition (+), while the adaptive feature-fusion module is implemented for optimal DF. Feature weights are assigned to the Avg2D pooling layers through the point-wise product (X), and subsequently concatenated (C) and flatten. The classification task is ultimately conducted with a fully connected (FC) layer, dropout and ‘Softmax’ function.

feature weights are assigned to these layers through point-wise product (or scalar multiplication), and subsequently concatenated and flatten for optimal DF. Lastly, we add a fully connected layer with dropout rate set to 0.2 and a ‘Softmax’ function for final land cover classification (Fig. 4). The C-CAP establishes 17 land cover classes in the U.S, but we grouped similar classes into 7 general categories to avoid unnecessary specificity and improve interpretability as suggested in similar studies (Pouliot et al., 2019; Spruce et al., 2014). In addition, we have included the ‘floodwater’ class derived from hydrodynamic simulations as indicated in the previous section. The resulting land cover and compound flood map has a spatial resolution of 30 m by setting an overlap (or stride) of 6 pixels in x- and y-direction. Note that we explicitly train the CNN & DF framework to separate floodwater from permanent water. Further details of the layers used in the CNN architecture are explained in Muñoz et al. (2021).

3.4. Model training /validation and evaluation of the CNN & DF framework

The land cover and flood mapping model can be trained with single, double and triple dataset combinations depending on data availability. The Savannah River estuary counts with all three input datasets (e.g., Landsat ARD, DEM and SAR), and is therefore suitable for training the framework with any possible dataset combinations in the southeast Atlantic coast. The sampling process consists of extracting patch images of 30×30 pixels (or 150×150 m) from pre- and post-flood imagery according to the C-CAP land cover and flood maps. Since some land cover classes are scarce in the training area (e.g., grass/bare land, shore and floodwater), we deal with unbalanced data with data augmentation, i.e., rotating the sample patches, and class weight computation prior to the sampling process. Moreover, we randomly separate training (80% or 17,980) and validation (20% or 4496) patches with a fixed seed value to ensure reproducibility.

The selected model optimizer and loss function are the stochastic gradient descent algorithm (SGD) with exponential decay and the sparse categorical cross-entropy, respectively. To avoid overfitting, we use 100 epochs with a callback ‘early stopping’ monitoring accuracy values and ‘patience’ option set to 10 epochs. The initial learning rate is set to 0.01 for all input datasets. The number of training epochs as well as the initial learning rate are selected from trial-and-error tests with randomly selected values ranging from 50 to 200 and 1e-4 to 0.1, respectively. In addition, we conducted fine-tuning of the CNN architecture with a smaller learning rate (1e-3) and identical model settings described above. Model weights resulting from the training process with dataset combinations and/or DF alternatives are conveniently stored for further transfer learning in the southeast Atlantic coast. The CNN & DF framework ultimately classifies patch images of 30×30 pixels

with a patch-based approach centered on a single pixel. Contrary to pixel-based approaches, patch-based analysis allows the CNN to learn contextual information from local spatial features of neighboring pixels (Carranza-García et al., 2019; Chen et al., 2017). Misclassification errors that may arise from patches located at the edge of two or more land cover classes are controlled by allowing the patch images to contain less than 10% (or < 90 pixels) of other land cover classes as suggested in Muñoz et al. (2021). Model validation is conducted with patch images of identical size obtained from C-CAP (2016–2017) and flood maps derived from hydrodynamic simulations of the Delft3D-FM model (Figs. 2f and 3b).

Lastly, we evaluate compound flood maps obtained from the CNN & DF framework with respect to two datasets: (i) USGS – high water marks, and (ii) maximum flood extent map of the CERA web mapper. Those maps and high water marks are conveniently masked with geospatial tools in order to span coastal counties of interest where flood inundation is evident (Fig. 1a). Although high water marks are indicative of flood inundation depth, we use point coordinates of those marks as a proxy of ‘ground truth’ flood areas within the coastal counties. We then conduct a pixel-based spatial analysis (30×30 m) to determine whether the flood maps of the CNN & DF framework and CERA match those point coordinates or not. Furthermore, we compare flood/non-flood areas in the coastal counties by measuring the agreement between the maps of the CNN & DF framework and CERA (Eq. (2)). The advanced fitness index (AFI) was first developed to compare inundated areas simulated with hydrodynamic models versus observed inundated areas of aerial imagery and SAR data (Bates and Roo, 2000), and eventually modified to compare both non-inundated and inundated areas (Munasinghe et al., 2018).

$$AFI = \frac{FA_{obs} \cap FA_{mod} + NFA_{obs} \cap NFA_{mod}}{A_{obs} \cup A_{mod}} \times 100 \quad (2)$$

where, FA_{obs} is flood area from observed imagery (e.g., floodwater class obtained from the CNN & DF framework), FA_{mod} is flood area simulated with large-scale hydrodynamic modeling (e.g., CERA map derived from ADCIRC model), NFA is non-flood area and A is the total area under analysis.

4. Results

4.1. Accuracy assessment

We evaluate the CNN & DF framework in terms of overall accuracy, Cohen's kappa coefficient, f1-score (macro) and f1-score per class (Table 2). Regarding the Landsat ARD imagery, the highest accuracies

Table 2

Accuracy assessment of data fusion alternatives for land cover classification and flood mapping in the Savannah River estuary.

Dataset	Band composite	Overall accuracy (%)	Cohen's kappa (%)	f1-score (macro) (%)	f1-score permanent water/floodwater (%)
ARD	All bands ^a	95.73	95.09	95.57	97.85/100
	R, G and B	87.28	85.38	86.06	96.10/100
	R, G and Nir	91.10	89.79	90.39	97.91/99.91
	Nir, Swir1 and Swir2	92.37	91.23	91.82	97.31/94.99
SAR	VH and VV ^b	86.48	84.47	86.00	98.25/83.73
DEM	Single band	77.45	74.03	74.96	98.70/85.51
ARD+SAR	All bands + VH and VV	96.37	95.84	96.31	98.38/100
	Nir, Swir1 and Swir2 + VH and VV	95.71	95.07	95.49	99.39/99.82
ARD+DEM	All bands + Single band	97.09	96.65	96.97	98.25/100
	Nir, Swir1 and Swir2 + Single band	96.62	96.12	96.49	99.18/100
SAR+DEM	VH and VV + single band	95.97	95.38	95.92	99.18/100
ARD+SAR+DEM	All bands + VH and VV + Single band	97.55	97.19	97.48	99.39/100
	Nir, Swir1 and Swir2 + VH and VV + Single band	97.24	96.83	97.13	99.39/100

Text with italic letters indicates the benchmark among the data fusion alternatives when all bands are included.

Text with bold letters highlights the (cost-effective) band composite that achieves the highest accuracy as compared to the other composites.

^a Red (R), Green (G), Blue (B), Near-infrared (Nir), Shortwave infrared (SWIR) 1 and 2.

^b Vertical (V) and horizontal (H) polarizations.

are observed when all six spectral bands are used in the framework. Nevertheless, this implies a heavy computation burden that might increase even more when implementing multi-source DF. To reduce computation burden and overcome graphics-processing-unit (GPU) memory usage limitation, we select the last band combination for further transfer learning in the southeast Atlantic coast. The rationale behind this selection is that Nir, Swir1 and Swir2 achieve the highest accuracies in both land cover and flood mapping (bold letters) as compared to the other band combinations (Table 2), and also allow for a relative easier interpretability of non-physical parameters. Note that we report the accuracies associated with all spectral bands and DF alternatives as a benchmark (italic letters).

Among the DF alternatives, the highest overall accuracy and f1-scores of permanent/flood water classes are achieved when ARD, SAR and DEM datasets are readily available and adequately fused. In absence of Landsat ARD imagery, or equivalently having scenes with cloud cover/shadow percentages above 20%, SAR and DEM datasets are a

suitable DF alternative as they achieve satisfactorily results with less than 1% difference with respect to the former alternative. The same percentage is obtained when ARD and DEM datasets are fused together. ARD and SAR dataset combination is less accurate (2%) than ARD, SAR and DEM together. The higher accuracy of the latter combination highlights the role of DEM data in the fusion process as elevation features combined with spectral and/or backscattering features help overcome misclassification errors associated with land cover classes having similar spectral or backscattering signatures. Nonetheless, in absence of highly detailed DEMs, the ARD and SAR dataset combination can still lead to comparable accuracies with respect to the ideal DF alternative (all datasets). Moreover, high overall accuracy results ($> 95\%$) obtained from all DF alternatives suggest that the CNN & DF framework can perform satisfactorily in other remote areas with limited data availability. It is noted that the proposed band selection (Nir, Swir1 and Swir2) and all six spectral bands achieve identical f1-scores in permanent water and floodwater classes.

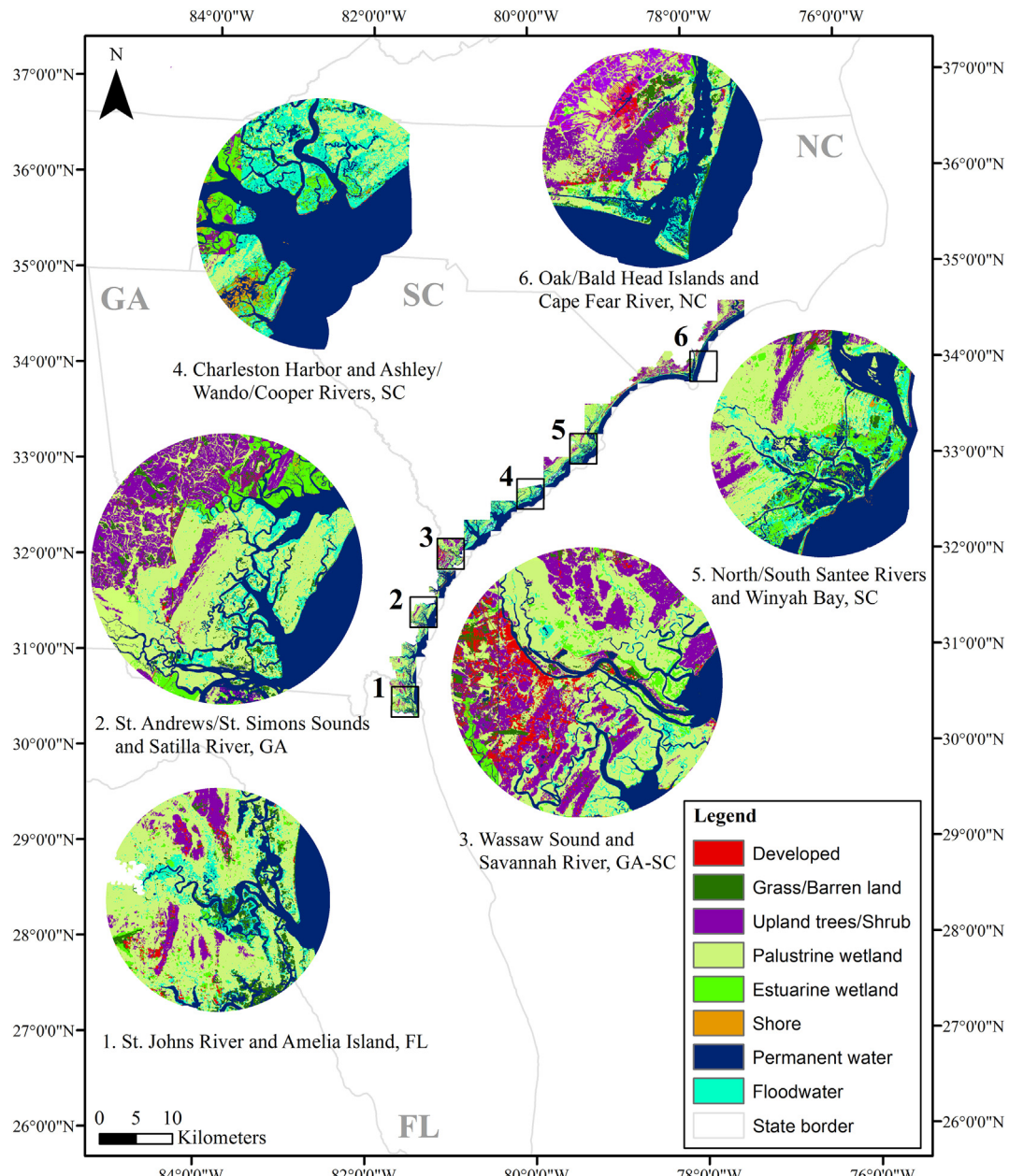


Fig. 5. Land cover classification and compound flood mapping in the southeast Atlantic coast of the U.S. Scale bar corresponds to the colored circles. Note that the CNN & DF model is able to discriminate permanent (dark-blue) and floodwater (cyan) classes.

4.2. Land cover and compound flood mapping

We use a transfer learning approach (e.g., model weights obtained from the pre-trained CNN & DF framework) to conduct land cover classification and compound flood mapping in the south east Atlantic coast based on available datasets (Table 1). Particularly, we focus our analysis on the most flood-impacted zones of the study area including coastal counties of northern Florida, Georgia, South Carolina and southern North Carolina (Fig. 5). The framework can efficiently separate permanent water from floodwater even though minor misclassification errors are observed among (dry) land cover classes. This is also noticeable in the confusion matrix of the training area (validation patches); specifically, the palustrine wetland class achieves the lowest producer's and user's accuracies (Table A1 in the Appendix).

In addition, we evaluate the performance of the CNN & DF framework with respect to hindcast flood guidance maps of CERA (Fig. 6). In the figure, red color highlights flood areas that match both our proposed framework and CERA maps. Flood areas obtained exclusively from the framework and CERA are shown with cyan and dark-blue, respectively. Note that the floodwater class is correctly delineated at most of the high water marks (yellow circles) in the southeast Atlantic coast. Specifically, we conduct a pixel-based spatial analysis to determine the number of high water marks that are correctly delineated with maps of the CNN & DF framework and CERA. Those results are reported as relative percentages with respect to the total number of marks available at each location (Table 3). Overall, the CNN & DF framework captures 39% of all USGS – high water marks distributed along the coastal counties (e.g., 393 marks). Note that this percentage is higher than the one calculated with the CERA map by a factor

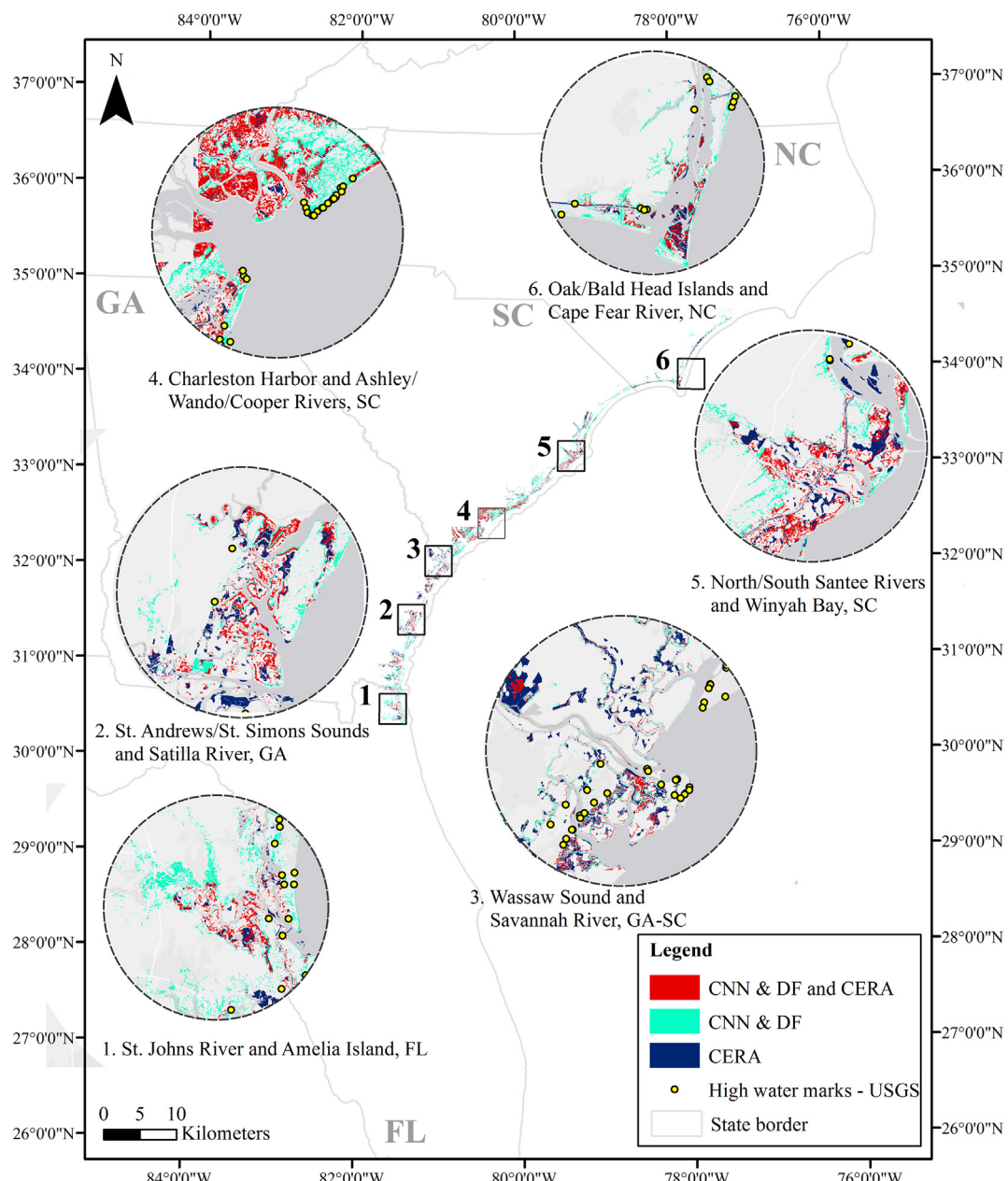


Fig. 6. Comparison of flood maps between the CNN & DF framework and the CERA. Red areas indicate agreement between both maps, while cyan and dark-blue areas indicate the opposite. Scale bar corresponds to the colored circles.

Table 3

Evaluation of the CNN & DF framework with USGS – high water marks (HWMs) and the advanced fitness index (AFI).

Location of main rivers, estuaries and islands	HWMs – CNN & DF (%)	HWMs – CERA (%)	AFI (%)
St. Johns River and Amelia Island, FL	31.58	5.26	82.16
St. Marys River and Cumberland Sound, GA	52.63	5.26	84.00
St. Andrew/St. Simons Sounds and Satilla River, GA ^a	16.67	27.78	66.56
Altamaha River and Sapelo Island, GA ^a	0.00	0.00	73.07
Ogeechee River and Ossabaw Islands, GA ^a	0.00	33.33	61.24
Wassaw Sound and Savannah River estuary, GA-SC ^a	7.14	42.86	68.08
St. Helena Sound and Coosaw River, SC	51.16	32.56	73.53
Hunting and St. Edisto Islands, SC	54.55	18.18	75.48
Charleston Harbor, Ashley/Cooper/Wando Rivers, SC	22.22	20.37	74.44
North/South Santee Rivers and Winyah Bay, SC	6.67	20.00	80.83
Waccamaw River, Long Bay and Myrtle Beach, SC	0.00	0.00	69.70
Atlantic Beach and North Myrtle Beach, SC	56.00	6.00	82.95
Little River, Bird Island and Ocean Isle Beach, NC	69.57	17.39	95.29
Oak/Bald Head Islands and Cape Fear River, NC	61.90	14.29	95.02
Zekes Island and Kure/Carolina Beach, NC	22.22	44.44	95.36
Masonboro Island and Wrightsville Beach, NC	9.09	9.09	92.51
Figure Eight Island and Topsail Beach, NC	22.22	22.22	91.97
North Topsail Beach and New River	10.00	0.00	96.34
Global	38.93	19.08	80.38

^a Landsat ARD, SAR and DEM datasets.

of 2. Comparisons of flood/non-flood areas between maps of the CNN & DF framework and CERA indicate an overall agreement of 80% (Table 3). All locations shown in the table count with SAR and DEM datasets except those marked with an asterisk that include Landsat ARD dataset with clouds and shadows less than 20% (see Section 2.2 for details). AFI ranges from 61% to 96% at selected rivers, estuaries and islands suggesting that the transfer learning approach with the CNN & DF framework is an efficient alternative for compound flood mapping at large-scale.

5. Discussion

5.1. Large-scale compound flood mapping

Advanced hydrodynamic modeling is a common approach for simulating physically-based processes such as compound flooding at large-scale (Dietrich et al., 2011; Muis et al., 2019; Vousdoukas et al., 2016; Wing et al., 2017). However, such an approach requires an adequate mesh resolution (e.g., order of meters) and a thorough model calibration to accurately represent CF in coastal to inland transition zones where flooding drivers interact (Bilskie and Hagen, 2018; Santiago-Collazo et al., 2019). An effective alternative that can complement current efforts in complex physical and dynamical modeling consists in leveraging DL models and transfer learning for post-event flood mapping. Transfer learning is an emerging and powerful technique for compound flood mapping and can help in flood hazard assessment of data scarce regions with only satellite-based data. In addition, DL and DF techniques can potentially aid in model parameter calibration and uncertainty reduction of flood hazard maps (Gude et al., 2020; Kabir et al., 2020b).

In this study, we propose a compound flood mapping strategy via multiclass land cover classification with CNNs and an adaptive DF approach (Fig. 4). The CNN & DF framework aims at reducing misclassification errors associated with land cover heterogeneities and underlying complexity. The f1-scores of permanent water and floodwater slightly improve according to the DF alternatives with maximum values of 99.39 and 100% for permanent water and floodwater, respectively (Table 2). We argue that such high accuracies result from a correct classification of the entire set of land cover classes as opposite to common approaches that rely on decision rules or threshold values for binary classification of flood/non-flood areas. In this regard, we ensure the framework correctly delineates floodwater areas without requiring

global or localized thresholds that may lead to over- or underestimation of flood extent and overfitting in the classification process (Liang and Liu, 2020). The selection of MHHW as ‘floodwater threshold’ in Delft3D-FM model simulations helps identify purely hurricane-induced and fluvial flooding from periodical flooding in wetlands and salt marshes, which are present in most estuaries and bays of the southeast Atlantic coast (Fig. 5). Particularly, the MHHW (referenced to the NAVD88) adds a physical meaning to the compound flood mapping process (e.g., floodwater training samples) and complements ‘abstract’ feature information extracted from multispectral, backscattering and elevation properties of the input datasets (Fig. 4).

5.2. Data fusion alternatives and limitations of the framework

The acquisition dates of SAR data are a few days later than the date/time of Hurricane Matthew's best track, and up to 5 days later in the case of Landsat ARD (Fig. 1a and Table 1). Flood recession is therefore of consideration as it may start a few hours later than the local peak storm surge, and so reduce the ability of the framework to delineate maximum flood extent and/or match post-flood high water marks collected in coastal counties (Table 3). Nonetheless, the compound effects of flood drivers do not necessarily coincide with the occurrence of the dominant flood driver (e.g., storm-surge), but usually with lag times of up to 7 days according to local-scale and global studies (Klerk et al., 2015; Moftakhar et al., 2017; Ward et al., 2018). In this regard, we expect fewer USGS – high water marks correctly identified with maps of the CNN & DF framework as well as an underestimation of flood inundation extent; especially at locations where the Landsat ARD dataset is available and fused (see rows with an asterisk in Table 3). This might also help explain the relatively low AFI values at locations that count with this lagged dataset. In contrast, we observe relatively high AFI values at locations where SAR and DEM datasets are fused since the former dataset is closer to the peak surge of Hurricane Matthew (Fig. 3a). Hindcast flood guidance maps derived from a large-scale hydrodynamic model (ADCIRC) and available via the CERA web mapper may also contain uncertainties leading to over- and underestimation of maximum flood extent. Particularly, these uncertainties in hydrodynamic modeling may have led to a lower global percentage of high water marks correctly matched (~19%) as compared to the proposed framework (~39%).

Although we could have used the CERA map as an additional input dataset of the CNN & DF framework, we intentionally left this map out

of the training process and used it for validation purposes instead. We therefore evaluate the performance of the framework without the help from a large-scale ADCIRC model, but focus our efforts on a local-scale hydrodynamic modeling (Delft3D-FM) of relatively shorter simulation time and transfer learning approach with pre-trained model weights. We show the CNN & DF framework achieves moderate-high accuracies overall in terms of high water marks and AFI percentages (Table 3) even with floodwater samples derived from the Savannah River estuary, GA. Hurricane Matthew considerably impacted this study area and led to the highest water surface level of the entire southeast Atlantic coast. Transfer learning from local to large-scale study areas is seen as a promising alternative for compound flood mapping given the complexity and computation burden associated with advanced hydrodynamic models at large-scale.

Limitations of the CNN & DF framework include the selection of a suitable deep learning architecture as well as analyses of the associated sources of uncertainty. In general, uncertainty from input data (satellite sensor's calibration and/or associated noise, data heterogeneity, and class-conditional distributions), model structure (deep learning architecture and/or number of 'deep' layers), and model parameters (loss function, learning rate, dropout rate, initial bias, number of epochs, etc.) can lead to misclassification and/or prediction errors. To overcome such limitations, we conduct pre-processing of input data (Section 3.1) as well as trial-and-error tests to find 'optimal' values for patch and kernel sizes, number of epochs and learning rate as suggested in several studies (Section 3.4). A thorough uncertainty analysis would demand a full study by itself given several sources of uncertainty and is therefore left for future studies. Moreover, the main goal of this study is to propose a framework based on DL and present it comprehensively.

6. Conclusion

The Atlantic hurricane season in the U.S. coasts is responsible for multiple deaths, severe damages to infrastructure and environmental impacts associated to compound flooding. Flood emergency managers and stakeholders are thus in need of real-time detailed flood maps for decision-making, prompt emergency response and coastal flood assessment. In this study, we presented a modified CNN & DF framework that integrates multi-source remotely sensed data and hydrodynamic model results to map compound flooding in the southeast Atlantic coasts of the U.S. The framework was trained in the Savannah River estuary, GA and achieved the highest accuracy results for all land cover classes when

fusing Landsat ARD, SAR and DEM datasets. In absence of Landsat ARD imagery, or equivalently having scenes with too many shadows and cloudy pixels, fusing SAR and DEM datasets emerged as a suitable alternative for compound flood mapping with accuracies of less than 1% difference with respect to the former alternative. The model weights of the pre-trained framework were used for transfer learning in coastal counties of the southeast Atlantic coast, and hence allowing for compound flood mapping at large-scale. Comparison of flood maps at locations with available USGS – high water marks resulted in a higher accuracy of the CNN & DF framework than hindcast flood guidance maps of CERA (factor of 2). Nevertheless, both maps showed an overall agreement greater than 80% in flood/non-flood areas suggesting that the framework can efficiently discriminate floodwater from permanent water classes. We highlight the usefulness of the CNN & DF framework for large-scale compound flood mapping, and its potential use for a thorough calibration of hydrodynamic models and uncertainty reduction in coastal flood hazard assessment. Future work is envisioned toward a comprehensive framework that provides not only accurate flood extent maps, but also inundation depth based on both deep learning and multi-source data fusion techniques. Likewise, uncertainty analysis of the proposed framework would demand a full study by itself given several sources of uncertainty and is therefore left for future studies.

CRediT authorship contribution statement

David F. Muñoz: Conceptualization, Methodology, Validation, Software, Visualization, Writing – review & editing. **Paul Muñoz:** Methodology, Software, Writing – review & editing. **Hamed Moftakhar:** Supervision, Writing – review & editing. **Hamid Moradkhani:** Supervision, Writing – review & editing.

Declaration of competing interest

The authors declare that they have no known competing financial interests or personal relationships that could have appeared to influence the work reported in this paper.

Acknowledgments

This study is partially funded by the National Science Foundation INFEWS Program (award EAR-1856054). Also, partial support was provided by USACE contract #W912HZ2020055.

Appendix A

Table A1

Confusion matrix of validation patches (20% of the dataset) resulting from Landsat ARD, SAR and DEM data fusion in the Savannah River estuary.

Class	Developed	Grass/Bare land	Upland trees/Shrub	Palustrine wetland	Estuarine wetland	Shore	Permanent water	Floodwater	User's acc. (%)
Developed	421	1	0	0	0	0	0	0	99.76
Grass/Bare land	1	540	0	0	0	0	0	0	99.82
Upland trees/Shrub	0	3	687	22	0	0	0	0	96.49
Palustrine wetland	0	3	30	416	19	0	0	0	88.89
Estuarine wetland	0	0	1	9	589	0	0	0	98.33
Shore	1	3	0	2	20	439	6	0	93.21
Permanent water	0	0	0	3	0	0	729	0	99.59
Floodwater	0	0	0	0	0	0	0	551	100
Producer's acc. (%)	99.53	98.18	95.68	92.04	93.79	100	99.18	100	OA (%): 97.24

References

- Anusha, N., Bharathi, B., 2020. Flood detection and flood mapping using multi-temporal synthetic aperture radar and optical data. *Egypt. J. Remote Sens. Space Sci.* 23, 207–219. <https://doi.org/10.1016/j.ejrs.2019.01.001>.
- Bates, P.D., Roo, A.P.J.D., 2000. A simple raster-based model for flood inundation simulation. *J. Hydrol.* 236, 54–77. [https://doi.org/10.1016/S0022-1694\(00\)00278-X](https://doi.org/10.1016/S0022-1694(00)00278-X).

Bevacqua, Maraun, D., Vousdoukas, M.I., Voukouvalas, E., Vrac, M., Mentaschi, L., Widmann, M., 2019. Higher probability of compound flooding from precipitation and storm surge in Europe under anthropogenic climate change. *Sci. Adv.* 5, eaaw5531. doi:<https://doi.org/10.1126/sciadv.aaw5531>.

Bevacqua, E., Vousdoukas, M.I., Shepherd, T.G., Vrac, M., 2020. Brief communication: the role of using precipitation or river discharge data when assessing global coastal compound flooding. *Nat. Hazards Earth Syst. Sci.* 20, 1765–1782. <https://doi.org/10.5194/nhess-20-1765-2020>.

- Bilskie, M.V., Hagen, S.C., 2018. Defining flood zone transitions in low-gradient coastal regions. *Geophys. Res. Lett.* 45, 2761–2770. <https://doi.org/10.1002/2018GL077524>.
- Canisius, F., Brisco, B., Murnaghan, K., Van Der Kooij, M., Keizer, E., 2019. SAR backscatter and InSAR coherence for monitoring wetland extent, flood pulse and vegetation: a study of the Amazon lowland. *Remote Sens.* 11, 720. <https://doi.org/10.3390/rs11060720>.
- Carranza-García, M., García-Gutiérrez, J., Riquelme, J.C., 2019. A framework for evaluating land use and land cover classification using convolutional neural networks. *Remote Sens.* 11, 274. <https://doi.org/10.3390/rs11030274>.
- Chaoach, N., Temimi, M., Hagen, S., Weishampel, J., Medeiros, S., Khanbilvardi, R., 2012. A synergetic use of satellite imagery from SAR and optical sensors to improve coastal flood mapping in the Gulf of Mexico. *Hydrol. Process.* 26, 1617–1628. <https://doi.org/10.1002/hyp.8268>.
- Chen, Y., Li, C., Ghamisi, P., Jia, X., Gu, Y., 2017. Deep fusion of remote sensing data for accurate classification. *IEEE Geosci. Remote Sens. Lett.* 14, 1253–1257. <https://doi.org/10.1109/LGRS.2017.2704625>.
- Chini, M., Hostache, R., Giustarini, L., Matgen, P., 2017. A hierarchical split-based approach for parametric thresholding of SAR images: flood inundation as a test case. *IEEE Trans. Geosci. Remote Sens.* 55, 6975–6988. <https://doi.org/10.1109/TGRS.2017.2737664>.
- Clement, M.A., Kilsby, C.G., Moore, P., 2018. Multi-temporal synthetic aperture radar flood mapping using change detection. *J. Flood Risk Manag.* 11, 152–168. <https://doi.org/10.1111/jfr3.12303>.
- Cohen, S., Raney, A., Munasinghe, D., Loftis, J.D., Molthan, A., Bell, J., Rogers, L., Galantowicz, J., Brakenridge, G.R., Kettner, A.J., Huang, Y.-F., Tsang, Y.-P., 2019. The floodwater depth estimation tool (FwDET v2.0) for improved remote sensing analysis of coastal flooding. *Nat. Hazards Earth Syst. Sci.* 19, 2053–2065. <https://doi.org/10.5194/nhess-19-2053-2019>.
- Couasnon, A., Eilander, D., Muis, S., Veldkamp, T.I.E., Haigh, I.D., Wahl, T., Winsemius, H.C., Ward, P.J., 2020. Measuring compound flood potential from river discharge and storm surge extremes at the global scale. *Nat. Hazards Earth Syst. Sci.* 20, 489–504. <https://doi.org/10.5194/nhess-20-489-2020>.
- Dalponte, M., Bruzzone, L., Gianelle, D., 2008. Fusion of hyperspectral and LIDAR remote sensing data for classification of complex Forest areas. *IEEE Trans. Geosci. Remote Sens.* 46, 1416–1427. <https://doi.org/10.1109/TGRS.2008.916480>.
- DeVries, B., Huang, C., Armston, J., Huang, W., Jones, J.W., Lang, M.W., 2020. Rapid and robust monitoring of flood events using Sentinel-1 and Landsat data on the Google earth engine. *Remote Sens. Environ.* 240, 111664. <https://doi.org/10.1016/j.rse.2020.111664>.
- Dhara, S., Dang, T., Parial, K., Lu, X.X., 2020. Accounting for uncertainty and reconstruction of flooding patterns based on multi-satellite imagery and support vector machine technique: a case study of can Tho City, Vietnam. *Water* 12, 1543. <https://doi.org/10.3390/w12061543>.
- Dietrich, J.C., Zijlema, M., Westerink, J.J., Holthuijsen, L.H., Dawson, C., Luettich, R.A., Jensen, R.E., Smith, J.M., Stelling, G.S., Stone, G.W., 2011. Modeling hurricane waves and storm surge using integrally-coupled, scalable computations. *Coast. Eng.* 58, 45–65. <https://doi.org/10.1016/j.coastaleng.2010.08.001>.
- Dietrich, J.C., Tanaka, S., Westerink, J.J., Dawson, C.N., Luettich, R.A., Zijlema, M., Holthuijsen, L.H., Smith, J.M., Westerink, L.G., Westerink, H.J., 2012. Performance of the unstructured-mesh, SWAN+ADCIRC model in computing hurricane waves and surge. *J. Sci. Comput.* 52, 468–497. <https://doi.org/10.1007/s10915-011-9555-6>.
- Dwyer, J.L., Roy, D.P., Sauer, B., Jenkerson, C.B., Zhang, H.K., Lymburner, L., 2018. Analysis ready data: enabling analysis of the Landsat archive. *Remote Sens.* 10, 1363. <https://doi.org/10.3390/rs10091363>.
- Eilander, D., Couasnon, A., Ikeyachi, H., Muis, S., Yamazaki, D., Winsemius, H., Ward, P.J., 2020. The effect of surge on riverine flood hazard and impact in deltas globally. *Environ. Res. Lett.* <https://doi.org/10.1088/1748-9326/ab8ca6>.
- Fang, Jiayi, Wahl, T., Fang, Jian, Sun, X., Kong, F., Liu, M., 2020. Compound flood potential from storm surge and heavy precipitation in coastal China. *Hydrology and Earth System Sciences Discussions*, pp. 1–24 <https://doi.org/10.5194/hess-2020-377>.
- Feng, Q., Liu, J., Gong, J., 2015. Urban flood mapping based on unmanned aerial vehicle remote sensing and random forest classifier—a case of Yuyao, China. *Water* 7, 1437–1455. <https://doi.org/10.3390/w7041437>.
- Feng, Q., Zhu, D., Yang, J., Li, B., 2019. Multisource hyperspectral and LiDAR data fusion for urban land-use mapping based on a modified two-branch convolutional neural network. *ISPRS Int. J. Geo Inf.* 8, 28. <https://doi.org/10.3390/ijgi8010028>.
- Flores-Anderson, A.J., Herndon, K.E., Thapa, R.B., Cherrington, E., 2019. The SAR handbook: comprehensive methodologies for Forest monitoring and biomass estimation.
- Gebrehiwot, A., Hashemi-Beni, L., Thompson, C., Kordjamshidi, P., Langan, T.E., 2019. Deep convolutional neural network for flood extent mapping using unmanned aerial vehicles data. *Sensors* 19, 1486. <https://doi.org/10.3390/s19071486>.
- Gianinetto, M., Villa, P., Lechi, G., 2006. Postflood damage evaluation using Landsat TM and ETM+ data integrated with DEM. *IEEE Trans. Geosci. Remote Sens.* 44, 236–243. <https://doi.org/10.1109/TGRS.2005.859952>.
- Gori, A., Lin, N., Smith, J., 2020. Assessing compound flooding from landfalling tropical cyclones on the North Carolina Coast. *Water Resour. Res.* 56, e2019WR026788. doi: <https://doi.org/10.1029/2019WR026788>.
- Gude, V., Corns, S., Long, S., 2020. Flood prediction and uncertainty estimation using deep learning. *Water* 12, 884. <https://doi.org/10.3390/w12030884>.
- Hendry, A., Haigh, I.D., Nicholls, R.J., Winter, H., Neal, R., Wahl, T., Joly-Laugel, A., Darby, S.E., 2019. Assessing the characteristics and drivers of compound flooding events around the UK coast. *Hydrol. Earth Syst. Sci.* 23, 3117–3139. <https://doi.org/10.5194/hess-23-3117-2019>.
- Hoeser, T., Bachofer, F., Kuenzer, C., 2020. Object detection and image segmentation with deep learning on earth observation data: a review—part II: applications. *Remote Sens.* 12, 3053. <https://doi.org/10.3390/rs12183053>.
- Hu, J., Shen, L., Sun, G., 2018. Squeeze-and-excitation networks. *Proceedings of the IEEE Conference on Computer Vision and Pattern Recognition*, pp. 7132–7141.
- Huang, C., Nguyen, B.D., Zhang, S., Cao, S., Wagner, W., 2017. A comparison of terrain indices toward their ability in assisting surface water mapping from Sentinel-1 data. *ISPRS Int. J. Geo Inf.* 6, 140. <https://doi.org/10.3390/ijgi6050140>.
- Kabir, S., Patidar, S., Pender, G., 2020a. A machine learning approach for forecasting and visualising flood inundation information. *Proceedings of the Institution of Civil Engineers – Water Management*, 1–15 <https://doi.org/10.1680/jwama.20.00000>.
- Kabir, S., Patidar, S., Xia, X., Liang, Q., Neal, J., Pender, G., 2020b. A deep convolutional neural network model for rapid prediction of fluvial flood inundation. *J. Hydrol.* 590, 125481. <https://doi.org/10.1016/j.jhydrol.2020.125481>.
- Klerk, Y., Winsemius, H.C., Verseveld, W.J., van Bakker, A.M.R., Diermanse, F.L.M., 2015. The co-incidence of storm surges and extreme discharges within the Rhine–Meuse Delta. *Environ. Res. Lett.* 10, 035005. <https://doi.org/10.1088/1748-9326/10/3/035005>.
- Li, Y., Zhang, H., Xue, X., Jiang, Y., Shen, Q., 2018. Deep learning for remote sensing image classification: a survey. *WIREs Data Mining and Knowledge Discovery* 8, e1264. <https://doi.org/10.1002/widm.1264>.
- Li, Y., Martinis, S., Wieland, M., 2019. Urban flood mapping with an active self-learning convolutional neural network based on TerraSAR-X intensity and interferometric coherence. *ISPRS J. Photogramm. Remote Sens.* 152, 178–191. <https://doi.org/10.1016/j.isprsjprs.2019.04.014>.
- Liang, J., Liu, D., 2020. A local thresholding approach to flood water delineation using Sentinel-1 SAR imagery. *ISPRS J. Photogramm. Remote Sens.* 159, 53–62. <https://doi.org/10.1016/j.isprsjprs.2019.10.017>.
- Lin, Y.N., Yun, S.-H., Bhardwaj, A., Hill, E.M., 2019. Urban flood detection with Sentinel-1 multi-temporal synthetic aperture radar (SAR) observations in a Bayesian framework: a case study for hurricane Matthew. *Remote Sens.* 11, 1778. <https://doi.org/10.3390/rs11151778>.
- Liu, B., Li, X., Zheng, G., 2019. Coastal inundation mapping from bitemporal and dual-polarization SAR imagery based on deep convolutional neural networks. *J. Geophys. Res. Oceans* 124, 9101–9113. <https://doi.org/10.1029/2019JC015577>.
- Luettich, R.A., Westerink, J.J., Scheffner, N.W., 1992. ADCIRC: an advanced three-dimensional circulation model for shelves, coasts, and estuaries. Report 1, Theory and methodology of ADCIRC-2DD1 and ADCIRC-3DL.
- Mahdianpari, M., Salehi, B., Rezaee, M., Mohammadimanesh, F., Zhang, Y., 2018. Very deep convolutional neural networks for complex land cover mapping using multispectral remote sensing imagery. *Remote Sens.* 10, 1119. <https://doi.org/10.3390/rs10071119>.
- Martinis, S., Twelte, A., Strobl, C., Kersten, J., Stein, E., 2013. A multi-scale flood monitoring system based on fully automatic MODIS and TerraSAR-X processing chains. *Remote Sens.* 5, 5598–5619. <https://doi.org/10.3390/rs5115598>.
- Martyr-Koller, R.C., Kernkamp, H.W.J., van Dam, A., van der Wegen, M., Lucas, L.V., Knowles, N., Jaffe, B., Fregoso, T.A., 2017. Application of an unstructured 3D finite volume numerical model to flows and salinity dynamics in the San Francisco Bay-Delta. *Estuar. Coast. Shelf Sci.* 192, 86–107. <https://doi.org/10.1016/j.ecss.2017.04.024>.
- Maxwell, A.E., Warner, T.A., Vanderbilt, B.C., Ramezan, C.A., 2017. Land cover classification and feature extraction from National Agriculture Imagery Program (NAIP) Orthoimagery: a review. *Photogramm. Eng. Remote. Sens.* 83, 737–747. <https://doi.org/10.14358/PERS.83.10.737>.
- Moftakhar, AghaKouchak, Sanders, A., Feldman, B.F., Sweet, D.L., Matthew, W., Luke, R.A., 2015. Increased nuisance flooding along the coasts of the United States due to sea level rise: past and future. *Geophys. Res. Lett.* 42, 9846–9852. <https://doi.org/10.1002/2015GL066072>.
- Moftakhar, Salvadori, AghaKouchak, G., Sanders, A., Matthew, B.F., 2017. Compounding effects of sea level rise and fluvial flooding. *PNAS* 114, 9785–9790. <https://doi.org/10.1073/pnas.1620325114>.
- Moftakhar, H.R., AghaKouchak, A., Sanders, B.F., Allaix, M., Matthew, R.A., 2018. What is nuisance flooding? Defining and monitoring an emerging challenge. *Water Resour. Res.* 54, 4218–4227. <https://doi.org/10.1029/2018WR022828>.
- Muis, S., Lin, N., Verlaan, M., Winsemius, H.C., Ward, P.J., Aerts, J.C.J.H., 2019. Spatiotemporal patterns of extreme sea levels along the western North-Atlantic coasts. *Sci. Rep.* 9, 3391. <https://doi.org/10.1038/s41598-019-40157-w>.
- Munasinghe, D., Cohen, S., Huang, Y.-F., Tsang, Y.-P., Zhang, J., Fang, Z., 2018. Intercomparison of satellite remote sensing-based flood inundation mapping techniques. *J. Am. Water Resour. Assoc.* 54, 834–846. <https://doi.org/10.1111/1752-1688.12626>.
- Muñoz, D.F., Cissell, J.R., Moftakhar, H., 2019. Adjusting emergent herbaceous wetland elevation with object-based image analysis, random Forest and the 2016 NLCD. *Remote Sens.* 11, 2346. <https://doi.org/10.3390/rs1120346>.
- Muñoz, D.F., Moftakhar, H., Moradkhani, H., 2020. Compound effects of flood drivers and wetland elevation correction on coastal flood Hazard assessment. *Water Resour. Res.* 56, e2020WR027544. doi:<https://doi.org/10.1029/2020WR027544>.
- Muñoz, D.F., Muñoz, P., Alipour, A., Moftakhar, H., Moradkhani, H., Mortazavi, B., 2021. Fusing multi-source data to estimate the effects of urbanization, sea level rise and hurricane impacts on long-term wetland change dynamics. *IEEE J. Select. Top. Appl. Earth Observ. Remote Sens.* 1–1. <https://doi.org/10.1109/JSTARS.2020.3048724>.
- Nandi, I., Srivastava, P.K., Shah, K., 2017. Floodplain mapping through support vector machine and optical/infrared images from Landsat 8 OLI/TIRS sensors: case study from Varanasi. *Water Resour. Manag.* 31, 1157–1171. <https://doi.org/10.1007/s11269-017-1568-y>.
- Olbert, A.J., Comer, J., Nash, S., Hartnett, M., 2017. High-resolution multi-scale modelling of coastal flooding due to tides, storm surges and rivers inflows. A Cork City example. *Coast. Eng.* 121, 278–296. <https://doi.org/10.1016/j.coastaleng.2016.12.006>.
- Pi, Y., Nath, N.D., Behzadan, A.H., 2020. Convolutional neural networks for object detection in aerial imagery for disaster response and recovery. *Adv. Eng. Inform.* 43, 101009. <https://doi.org/10.1016/j.aei.2019.101009>.

- Potapov, P., Hansen, M.C., Kommareddy, I., Kommareddy, A., Turubanova, S., Pickens, A., Adusei, B., Tyukavina, A., Ying, Q., 2020. Landsat analysis ready data for global land cover and land cover change mapping. *Remote Sens.* 12, 426. <https://doi.org/10.3390/rs12030426>.
- Pouliot, D., Latifovic, R., Pasher, J., Duffe, J., 2019. Assessment of convolution neural networks for wetland mapping with Landsat in the Central Canadian boreal forest region. *Remote Sens.* 11, 772. <https://doi.org/10.3390/rs11070772>.
- Qiu, S., Lin, Y., Shang, R., Zhang, J., Ma, L., Zhu, Z., 2019a. Making Landsat time series consistent: evaluating and improving Landsat analysis ready data. *Remote Sens.* 11, 51. <https://doi.org/10.3390/rs11010051>.
- Qiu, S., Zhu, Z., He, B., 2019b. Fmask 4.0: improved cloud and cloud shadow detection in Landsats 4–8 and Sentinel-2 imagery. *Remote Sens. Environ.* 231, 111205. <https://doi.org/10.1016/j.rse.2019.05.024>.
- Rad, A.M., Kreitler, J., Sadegh, M., 2021. Augmented normalized difference water index for improved surface water monitoring. *Environ. Model. Softw.*, 105030 <https://doi.org/10.1016/j.envsoft.2021.105030>.
- Reynolds, M.S., 2016. *Savannah River. South Carolina Encyclopedia*.
- Rezaee, M., Mahdianpari, M., Zhang, Y., Salehi, B., 2018. Deep convolutional neural network for complex wetland classification using optical remote sensing imagery. *IEEE J. Select. Top. Appl. Earth Observ. Remote Sens.* 11, 3030–3039. <https://doi.org/10.1109/JSTARS.2018.2846178>.
- Roelvink, J.A., Van Banning, G., 1995. Design and development of DELFT3D and application to coastal morphodynamics. *Oceanogr. Lit. Rev.* 11, 925.
- Santiago-Collazo, F.L., Bilskie, M.V., Hagen, S.C., 2019. A comprehensive review of compound inundation models in low-gradient coastal watersheds. *Environ. Model. Softw.* 119, 166–181. <https://doi.org/10.1016/j.envsoft.2019.06.002>.
- Sarker, C., Mejias, L., Maire, F., Woodley, A., 2019. Flood mapping with convolutional neural networks using Spatio-contextual pixel information. *Remote Sens.* 11, 2331. <https://doi.org/10.3390/rs11192331>.
- Seabrook, C., 2006. *Savannah River. New Georgia Encyclopedia. Geography & Environment, Major River Systems*.
- Singh, A., Singh, K.K., 2017. Satellite image classification using genetic algorithm trained radial basis function neural network, application to the detection of flooded areas. *J. Vis. Commun. Image Represent.* 42, 173–182. <https://doi.org/10.1016/j.jvcir.2016.11.017>.
- Song, J.Y., Alipour, A., Moftakhar, H., Moradkhani, H., 2020. Toward a more effective hurricane hazard communication. *Environ. Res. Lett.* <https://doi.org/10.1088/1748-9326/ab875f>.
- Spruce, J.P., Smoot, J.C., Ellis, J.T., Hilbert, K., Swann, R., 2014. Geospatial method for computing supplemental multi-decadal US coastal land use and land cover classification products, using Landsat data and C-CAP products. *Geocarto International* 29, 470–485. <https://doi.org/10.1080/10106049.2013.798357>.
- Stewart, S.R., 2017. Hurricane Matthew. National Hurricane Center (NHC). Tropical cyclone report. https://www.nhc.noaa.gov/data/tcr/AL142016_Matthew.pdf.
- Sweet, W.W.V., Dusek, G., Obeysekera, J.T.B., Marra, J.J., 2018. Patterns and projections of high tide flooding along the US coastline using a common impact threshold.
- Tam, T.H., Abd Rahman, M.Z., Harun, S., Hanapi, M.N., Kaoje, I.U., 2019. Application of satellite rainfall products for flood inundation modelling in Kelantan River Basin, Malaysia. *Hydrology* 6, 95. <https://doi.org/10.3390/hydrology6040095>.
- Thomas, A., Dietrich, J., Asher, T., Bell, M., Blanton, B., Copeland, J., Cox, A., Dawson, C., Fleming, J., Luettich, R., 2019. Influence of storm timing and forward speed on tides and storm surge during hurricane Matthew. *Ocean Model.* 137, 1–19. <https://doi.org/10.1016/j.ocemod.2019.03.004>.
- Tien Bui, D., Hoang, N.-D., Martínez-Álvarez, F., Ngo, P.-T.T., Hoa, P.V., Pham, T.D., Samui, P., Costache, R., 2020. A novel deep learning neural network approach for predicting flash flood susceptibility: a case study at high frequency tropical storm area. *Sci. Total Environ.* 701, 134413. <https://doi.org/10.1016/j.scitotenv.2019.134413>.
- Uddin, K., Matin, M.A., Meyer, F.J., 2019. Operational flood mapping using multi-temporal Sentinel-1 SAR images: a case study from Bangladesh. *Remote Sens.* 11, 1581. <https://doi.org/10.3390/rs11131581>.
- Voudoukas, M.I., Voukouvalas, E., Mentaschi, L., Dottori, F., Giardino, A., Bouziotas, D., Bianchi, A., Salamon, P., Feyen, L., 2016. Developments in large-scale coastal flood hazard mapping. *Nat. Hazards Earth Syst. Sci.* 16, 1841–1853. <https://doi.org/10.5194/nhess-16-1841-2016>.
- Wahl, Jain, Bender, S., Meyers, J., Luther, S.D., 2015. Increasing risk of compound flooding from storm surge and rainfall for major US cities. *Nat. Clim. Chang.* 5, 1093–1097. <https://doi.org/10.1038/nclimate2736>.
- Wang, Y., Colby, J.D., Mulcahy, K.A., 2002. An efficient method for mapping flood extent in a coastal floodplain using Landsat TM and DEM data. *Int. J. Remote Sens.* 23, 3681–3696. <https://doi.org/10.1080/01431160110114484>.
- Wang, J., Yi, S., Li, M., Wang, L., Song, C., 2018. Effects of sea level rise, land subsidence, bathymetric change and typhoon tracks on storm flooding in the coastal areas of Shanghai. *Sci. Total Environ.* 621, 228–234. <https://doi.org/10.1016/j.scitotenv.2017.11.224>.
- Ward, P.J., Couasnon, A., Eilander, D., Haigh, I.D., Hendry, A., Muis, S., Veldkamp, T.I.E., Winsemius, H.C., Wahl, T., 2018. Dependence between high sea-level and high river discharge increases flood hazard in global deltas and estuaries. *Environ. Res. Lett.* 13, 084012. <https://doi.org/10.1088/1748-9326/aad400>.
- Wing, O.E.J., Bates, P.D., Sampson, C.C., Smith, A.M., Johnson, K.A., Erickson, T.A., 2017. Validation of a 30 m resolution flood hazard model of the conterminous United States. *Water Resour. Res.* 53, 7968–7986. <https://doi.org/10.1002/2017WR020917>.
- Wu, W., McInnes, K., O'Grady, J., Hoeke, R., Leonard, M., Westra, S., 2018. Mapping dependence between extreme rainfall and storm surge. *J. Geophys. Res. Oceans* 123, 2461–2474. <https://doi.org/10.1002/2017JC013472>.
- Xu, Y., Du, B., Zhang, L., Cerra, D., Pato, M., Carmona, E., Prasad, S., Yokoya, N., Hänsch, R., Le Saux, B., 2019. Advanced multi-sensor optical remote sensing for urban land use and land cover classification: outcome of the 2018 IEEE GRSS data fusion contest. *IEEE J. Select. Top. Appl. Earth Observ. Remote Sens.* 12, 1709–1724. <https://doi.org/10.1109/JSTARS.2019.2911113>.
- Zoka, M., Psomiadis, E., Dercas, N., 2018. The complementary use of optical and SAR data in monitoring flood events and their effects. *Proceedings* 2, 644. <https://doi.org/10.3390/proceedings2110644>.
- Zscheischler, J., Martius, O., Westra, S., Bevacqua, E., Raymond, C., Horton, R.M., van den Hurk, B., AghaKouchak, A., Jézéquel, A., Mahecha, M.D., Maraun, D., Ramos, A.M., Ridder, N.N., Thiery, W., Vignotto, E., 2020. A typology of compound weather and climate events. *Nature Rev. Earth Environ.* 1, 333–347. <https://doi.org/10.1038/s43017-020-0060-z>.